AGU PUBLICATIONS

Geophysical Research Letters

Supporting Information for

Replenishment of near-surface water ice by impacts into Ceres' volatile-rich crust: Observations by Dawn's Gamma Ray and Neutron Detector

T. H. Prettyman[1], N. Yamashita[1], M. E. Landis[2], J. C. Castillo-Rogez[3], N. Schörghofer[1], C. M. Pieters[1,4], Sizemore[1], H. Hiesinger[5], S. Marchi[6], H. Y. McSween[7], R. S. Park[3], M. J. Toplis[8], C. A. Raymond[3], C. T. Russell[9]

[1]Planetary Science Institute, Tucson, AZ. [2]Laboratory for Atmospheric and Space Physics, University of Colorado, Boulder, CO. [3]Jet Propulsion Laboratory, California Institute of Technology, Pasadena, CA. [4]Brown University, Providence, RI. [5]Institut für Planetologie, Westfälische Wilhelms-Universität Münster, Münster, Germany. [6]Southwest Research Institute, Boulder, CO. [7]University of Tennessee, Knoxville, TN. [8]L'Institut de Recherche en Astrophysique et Planétologie (University of Toulouse, UT3, CNRS), Toulouse, France. [9]University of California Los Angeles, Los Angeles, CA.

Contents of this file

Text S1 to S4
Figures S1 to S3

Introduction

The supplementary information describes the collection, reduction, and mapping of high spatial resolution data acquired by the Gamma Ray and Neutron Detector (GRaND) in Dawn final mission phase (Text S1 and S2).

Text S3 describes a mineral mixing model used to estimate the concentration of hydrogen within and around Occator crater based on mineral maps derived from data acquired by Dawn's Visible and Infrared Mapping Spectrometer (VIR).

Text S4 provides an overview of the thermophysical ice stability model used to support the interpretation of the data.

Figure S1 demonstrates that the high-resolution GRaND data are sensitive to the presence of hydrogen within the interior of Occator crater and the ejecta blanket.

Figure S2 shows the longitudinal dependence of crater density and hydrogen concentration.

Figure S3 compares the pattern of large craters with the distribution of hydrogen.

Text S1. Data and corrections

The GRaND data used in this study are available from the Planetary Data System (PDS) in PDS4 format:

https://sbn.psi.edu/pds/resource/dawn/dawngrandPDS4.html

In Dawn's final mission phase, GRaND acquired data in a highly eccentric orbit with a south-to-north trajectory around Ceres. The orbit was in a 3:1 resonance with Ceres (27h orbital period), which enabled acquisition of data along a selected meridian. The periapsides drifted along a great circle, starting in the western hemisphere north of Occator crater, gradually moving southward along the 240E meridian and crossing into the eastern hemisphere. The last data were acquired north of the equator in the eastern hemisphere along the antimeridian (60E) (Fig. 1a).

Data acquired between 8-Jun and 26-Oct of 2018, just prior to end-of-mission (1-Nov) were used. During this time, the spacecraft completed 123 eccentric orbits, with periapsides ranging from less than 30 km near the equator to about 55 km near the South Pole (Fig. 1b). Data from 10 orbits for which the main antenna was Earth-pointed were discarded. The remaining 113 orbits were used in the analysis, which included 60690 science data records. Of these, 540 records (0.9%) were flagged as invalid and removed, leaving 60,145 data records for use in the analysis. To ensure ample spatial sampling of the surface, the accumulation time for science data records was commanded to 35s for altitudes below about 1200 km. At higher altitudes, the accumulation time was set to 455s.

The data were acquired under quiet Sun conditions. No data were discarded due to solar activity. Following previous work (Prettyman et al., 2012; Prettyman et al., 2017), the GRaND triples and higher order coincidence counter (triples+) was used as a proxy for the flux of galactic cosmic rays, which interact with the regolith to produce gamma-rays and neutrons. At altitudes greater than a few body radii, contributions from secondary particles produced by cosmic rays are negligible. The altitude of apoapsis was about 4000 km (8.5 body radii), which enabled variations in the flux of galactic cosmic rays to be monitored every orbit. The triples+ rate measured at altitudes >6 body radii was resampled via linear interpolation to determine the variations in the cosmic ray flux for the entire time series.

At low altitudes (within a few body radii), thermal and epithermal neutrons originating from Ceres' surface interact with GRaND's +Z lithium-loaded glass scintillator via the $^{6}Li(n,\alpha)$ reaction. This reaction makes a peak in the CAT1 pulse height spectrum, which can be analyzed to determine the reaction rate (Prettyman et al., 2011). The peak area was determined for each science accumulation interval by subtracting a background spectrum measured at high altitude from a region-of-interest containing the peak (see Fig. 1c and Prettyman et al., 2017, supplement). For each measurement, the background spectrum was normalized to the continuum determined for each measurement from counts in a high energy region above the peak. The shape of the background was assumed to be the same for all measurements and was determined from high altitude measurements. The same approach for peak extraction was used in all previous studies (Prettyman et al., 2011; 2012; 2017).

The peak areas were divided by live time and corrections were applied to remove variations in the flux of galactic cosmic rays and measurement geometry. This produced a time-series of corrected interaction rates sensitive only to variations in surface composition. For measurement geometry, the ^{6}Li(n,α) interaction rates were calculated at the mid-point location of each accumulation interval assuming the composition of Ceres' was homogeneous with a CI chondrite composition. The leakage current of neutrons (energy-angle distribution) for an arbitrary surface parcel was calculated using the Monte Carlo N-Particle eXtended transport code (McKinney et al., 2006). The Monte Carlo algorithm by Prettyman et al. (Prettyman et al., 2017; 2019) was used to model the response of the instrument to leakage neutrons at each orbital location, accounting for Ceres' shape and topography using a polygonal shape model determined from Framing Camera images using stereophotoclinometry (Park & Buccino, 2018; Park et al., 2019). The shape model was decimated to minimize compute times at high altitudes, where the instrument resolution is broader than the scale of surface features. For altitudes lower than 200 km, the mesh was decimated from 5123 to 2563 quadrilaterals, such that the mean distance between mesh points was about 3 km. This is sufficient to model the geometry of large-scale features such as Occator crater. Normalizing the measurements to simulated counts for a homogeneous surface removes artifacts of Ceres' shape and topography.

Text S2. Hydrogen mapping

The corrected ^{6}Li(n,α) interaction rates were mapped onto the surface of Ceres using a circle superposition algorithm that accounts for variations in the spatial resolution of the instrument with altitude. Individual measurements are sensitive to the composition within an approximately circular surface region centered at the subsatellite point. The diameter of the circle is given by the spatial resolution of the spectrometer, which varies in proportion to altitude (e.g., Prettyman et al., 2019). For each measurement, the corrected interaction rate is uniformly distributed on the surface within the corresponding circle. The surface contributions from all the measurements are then averaged together to form a map.

Circle superposition approximates the double convolution of surface features by the response function of the spectrometer, which is a conservative approach for detection of variations in surface composition. The method is a robust extension of mapping algorithms that place measurements at the subsatellite point (Maurice et al., 2004). Circle superposition accounts for the widely varying spatial influence and limited spatial sampling of the measurements acquired in the eccentric orbits.

The maps presented in Figs. 2 and 3 were constructed from 5088 measurements acquired below 100 km altitude with the instrument pointed to within 20 degrees of body center. For the selected measurements, the average pointing angle was 4.8 degrees, with a population standard deviation of 3.5 degrees. Most of the data (98%) was acquired with a pointing angle <12 degrees, with 94% within 10 degrees and 59% within 5 degrees. This is consistent with the quality of the pointing data used for hydrogen mapping in LAMO, for which the cutoff was 12 degrees (Prettyman et al., 2017).

Selection of measurements made below 100 km provided ample spatial coverage to examine global latitude variations observed previously in LAMO (Prettyman et al., 2017), with at least 3× higher spatial resolution. We used 1.5 as the factor relating altitude to spatial resolution, consistent with previous studies of low-altitude data sets (Haines et al., 1978; Lawrence et al., 2003; Prettyman et al., 2009), and conservatively larger than predicted for the lithium-loaded glass scintillator at LAMO altitudes (Prettyman et al., 2019). Map values within the point cloud are insensitive to moderate variations in the scaling factor. Mapped variations in regions outside the point cloud are an extrapolation of the data and may not be as accurate as points inside the cloud. Regions with high confidence are bounded by white contours in Figs. 2 and 3. Points within this region have been sampled at least 50 times. The maximum spatial resolution (minimum full width at half maximum arc length on the surface) supported by the data is about 50 km, given the minimum altitude sampled was about 30 km. This scale is indicated by the circle in Fig. 2c.

The distribution of hydrogen was determined from the mapped corrected interaction rates using the method described by Prettyman et al. (2017). For comparison, the counting data within 20 degrees of the equator were normalized to match the values acquired previously in LAMO. This accounted for differences in counting rates resulting from changes in instrument settings, drifts in gain, and changing solar conditions between LAMO and high-resolution observations made near the end of the mission. Hydrogen concentrations derived from thermal and epithermal counting data are subject to systematic contributions from other elements. Based on modeling of Ceres analog materials, this source of uncertainty is smaller than 1 wt.% eq. H_2O (Prettyman et al., 2017).

The statistical uncertainty (1-sigma) in mapped hydrogen concentrations was determined using Monte Carlo error propagation, given estimates of the uncertainty in the measurements. The circle superposition algorithm was applied to 100 random samples of the time-series counting data. The population standard deviation is indicated by the vertical lines in Fig. 2b.

Text S3. Mineral mixing model

Maps of mineral mixing fractions in the Occator region were determined from VIR spectra by (Raponi et al., 2019) by least squares fitting of spectral end-members. These included Mg-, Al-, and NH_4-bearing phyllosilicates, Mg- and Na-carbonates, ammonium chloride, and a dark component. Following previous studies (Marchi et al., 2019; McSween et al., 2017; Prettyman et al., 2017; 2019), the reported mixing fractions were interpreted as volume fractions, which were used to determine hydrogen concentrations given approximate mineral structural formulae and densities. A map of hydrogen concentrations derived from VIR mineralogy is shown in Fig. 3a.

Note that the dark component is spectrally featureless in the near infrared, consistent with a mixture of magnetite, troilite, and partially hydrated, amorphous carbon (De Sanctis et al., 2015); however, the spectral mixing fraction for this component is very high outside the faculae, greater than 0.9 in some locations. With such high mixing fractions, no combination of spectrally featureless minerals can match ice-free concentrations of hydrogen and iron determined by GRaND. Instead, we modeled the dark component as the global average composition inferred simultaneously from GRaND and VIR data (Table 1, Case B of Marchi et al. (2019), which includes featureless components as well as contributions from hydrated minerals and carbonates. This gives the correct hydrogen content for dark materials representative of the global regolith, while allowing variability in hydrogen contributions from specific minerals identified by (Raponi et al., 2019) within the Occator region. Our ad hoc approach for estimating hydrogen concentrations is justified given the large uncertainties involved in interpreting VIR-derived spectral mixing fractions as mineral abundances (McSween et al., 2017).

The VIR-derived hydrogen map (Fig. 3a) only includes lattice water and hydrogen in amorphous carbon. At depths greater than the optical surface, bound water (i.e., to salts and in the interlayer of clay minerals) may be present along with water ice. The mineral mixing model results in relatively low concentrations of hydrogen in the faculae (as low as 8 wt.% eq. H_2O) compared to their dark surroundings (about 17 wt.% eq. H_2O).

Text S4. Thermophysical model

Thermophysical models for water ice stability were run based on a temperature model (Landis et al., 2017; Landis et al., 2019) utilizing orbital parameters determined by the Dawn mission. Our model matches other numerical calculations for Ceres surface and subsurface temperatures (Prettyman et al., 2017; Schorghofer, 2016). The modeled temperatures were used in a Knudsen-diffusion model previously developed for airless bodies (Schorghofer, 2008). The diffusive loss of water vapor determines the thickness of regolith that builds up, and further buries the ice-bearing layer. The following parameters and assumptions were used:

- Grain sizes from the analysis of VIR data for lobate deposits on the floor of Occator crater and the ejecta blanket (~110- and 70-μm, respectively) (Raponi et al., 2019) were used to estimate the vapor diffusion coefficient (see Fig. 3b).
- Thermal inertia of 15 SI units for the over-lying lithic sublimation lag (Rivkin et al., 2011) is used for the thermal model.
- Regolith surface single-scattering albedo of 0.09 (Carrozzo et al., 2018; Li et al., 2016).
- Obliquity, argument of perihelion from Dawn mission results (Russell et al., 2016).
- Depth-to-ice values are not significantly affected by the ~25 kyr obliquity cycles over the lifetime of Occator (Landis et al., 2017; Schorghofer, 2016).
- Shadowing from crater walls is negligible due to Occator's relatively large diameter and relatively flat floor.
- The initial sublimation lag depth is 3 cm, which represents a barrier to diffusion. This lag depth is also many times the diurnal skin depth in Ceres' desiccated regolith. We assume the temperature of the ice is equal to the annual average surface temperature.

To estimate water loss from hydrated salts, we modified the model by assuming (1) the buried water-bearing salt was natron ($Na_2CO_3 \cdot 10H_2O$), (2) the temperature of the natron was equal to the annual average surface temperature calculated for the regolith given the aforementioned parameters, and (3) all water molecules released from natron are lost instantaneously (the molecules did not condense to form ice or rehydrate the natron). We calculated the salt dehydration rate using the Arrhenius equation with constants derived from experiments of natron dehydration under Europa-like conditions (McCord et al., 2001). We found that at Occator crater, natron within the subsurface dehydrated on short timescales compared to the crater's estimated age of 20 Myr (Scully et al., 2019). This is consistent with the detection of only dehydrated sodium carbonate at Occator (Raponi et al., 2019). This supports the conclusion that hydrated sodium carbonate is unlikely to be a major contributor of water in the shallow sub-surface compared to water ice.

Recent work (Bu et al., 2018a; Bu et al., 2018b) has suggested that the dehydration of salts on Ceres depends also on grain size. It suggests that the grain sizes used in McCord et al. (2001), were large enough to add additional dehydration time due to the diffusion of water vapor through the grain itself. Therefore, dehydration times based on constants for the Arrhenius model from McCord et al. (2001), are possibly only upper limits.

Other hydrated salts such as hydrohalite ($NaCl \cdot 2H_2O$), which was detected by VIR in Ceralia Facula (De Sanctis et al., 2020), and nahcolite ($NaHCO_3$), which degrades to form $NaCO_3$ under conditions present on Ceres' surface (Zolotov, 2017), are not likely a significant source of H. For example, even if nahcolite were concentrated in the shallow subsurface, it could account for no more than 11 wt.% equivalent H_2O. Experiments and modeling indicate the dehydration times for these minerals are also short compared to geologic time (Bu et al., 2018a; Bu et al., 2018b; Zolotov, 2017). Without the high pressures needed to re-hydrate these minerals, it is unlikely that they contribute as much hydrogen as water ice in the Occator region.

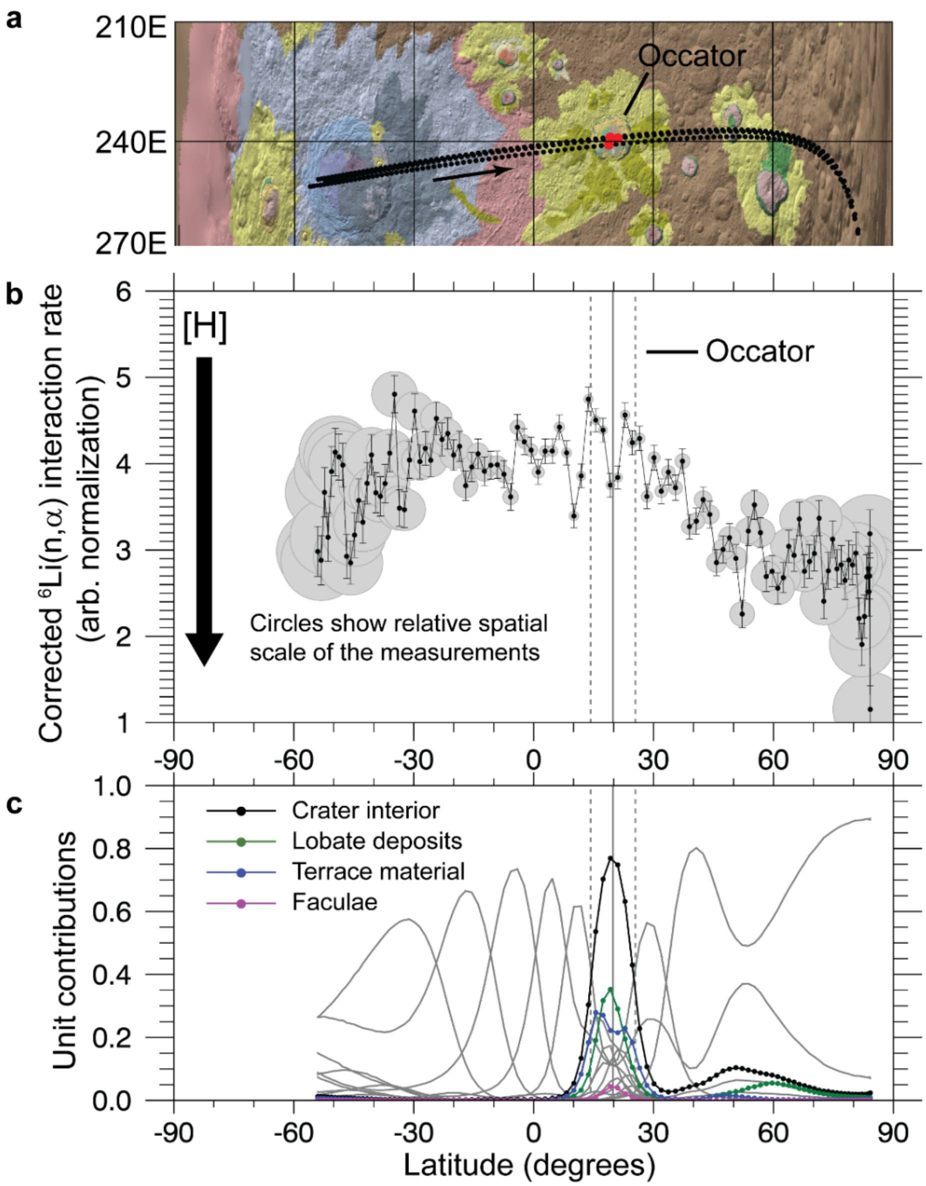

Figure S1. Spatial sensitivity of GRaND to geologic units within Occator crater. (a) Three orbits with nearly identical trajectories passing through the center of Occator crater are superimposed on a geologic map of Ceres (Williams et al., 2019). Locations of measurement center points (black circles) are plotted. The points of closest approach (about 35-km altitude) are highlighted in red. **(b)** The measured ^{6}Li(n,α) interaction rate averaged over the three orbits is shown (error bars indicate 1σ statistical precision). The dip within the crater boundary (dashed lines) is interpreted as elevated [H] within the crater interior. **(c)** A simulation of the response of GRaND to neutrons emitted from geologic units shows that the instrument is sensitive to the composition of the crater interior. The contribution from the faculae is negligible compared to lobate deposits and terrace material, which are possible locations for subsurface ice.

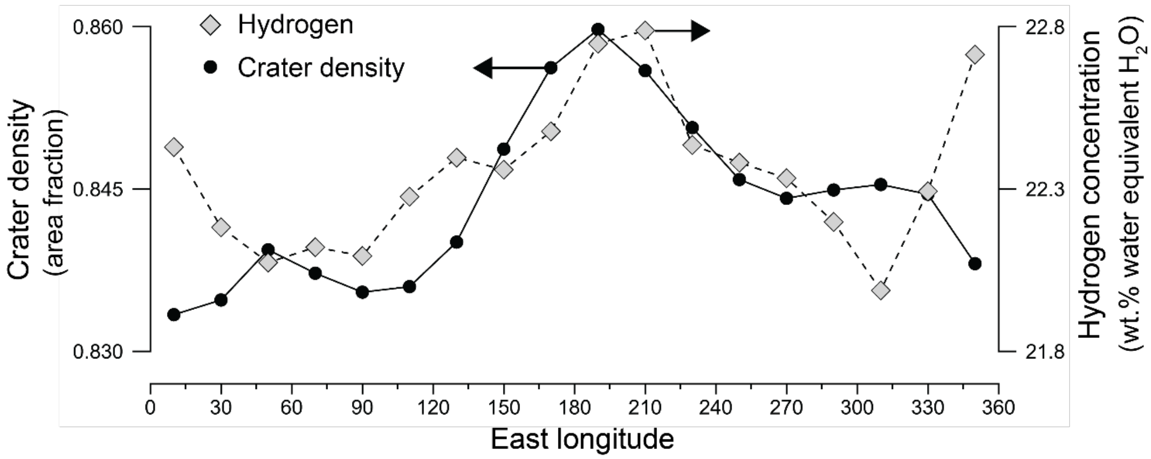

Figure S2. Longitudinal dependence of large craters and hydrogen concentration. The chart shows averages of the 20-degree equal area maps of crater density and hydrogen concentration (Fig. 4a) taken along meridians separated by 20 degrees longitude. The longitudinal variation in hydrogen concentration with crater density is correlated ($r = 0.55$). Given the coefficient of determination ($r^2 = 0.30$), the variation in hydrogen concentration is reduced by 30% when crater density is used as a predictor. As described in the main text, both crater density and hydrogen concentration have a broad maximum near 180E longitude.

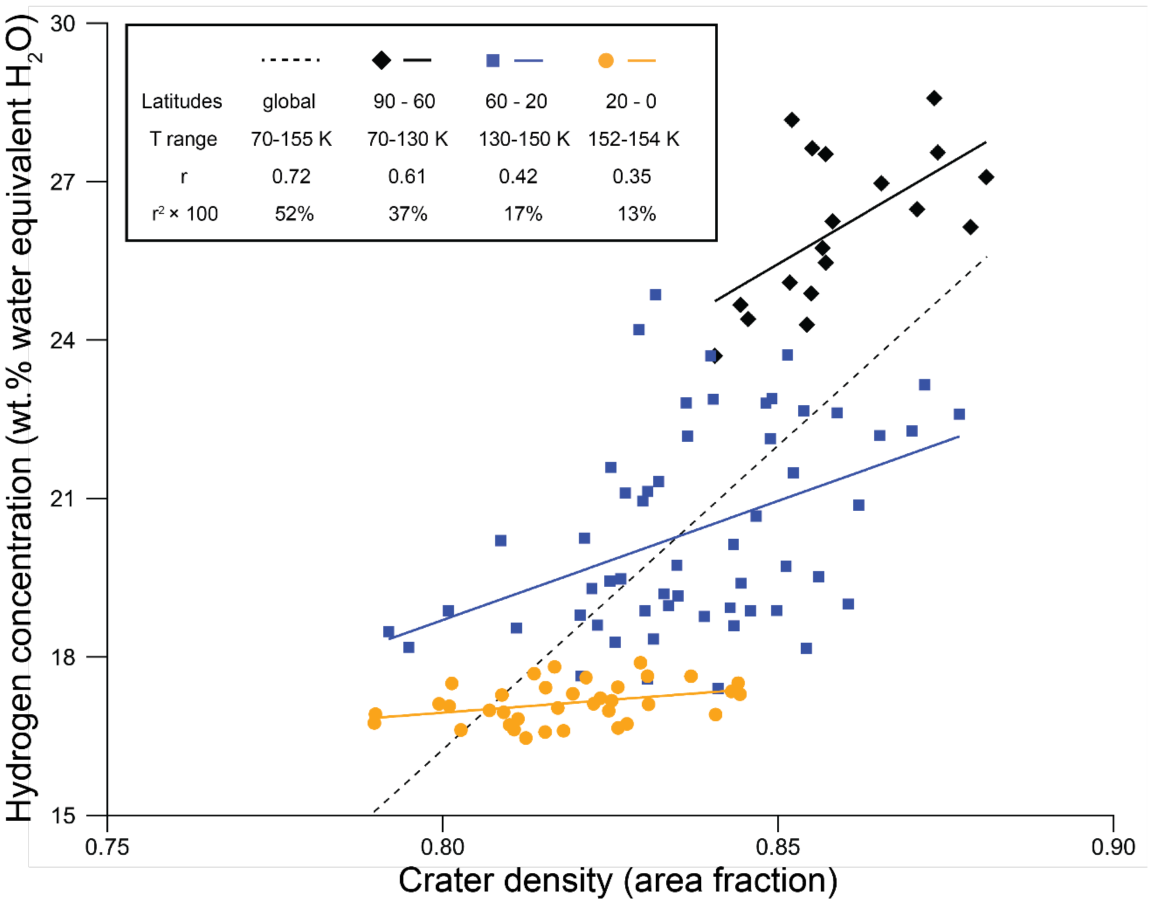

Figure S3. Comparison of the pattern of large craters and the distribution of hydrogen. Scatter plot of the density of large craters (20-100 km diameter) versus the concentration of hydrogen using data presented in Fig. 4a (see caption for the definition of crater density and data sources). The coefficient of determination (r^2) indicates strength of correlation and gives the fractional reduction in the variability of hydrogen that occurs when crater density is used as a predictor (see legend). The correlation is strong when all data points are considered; however, the concentration of hydrogen sensed by GRaND depends on the depth of subsurface water ice, which is controlled by near-surface temperature. Annual averaged surface temperatures, which vary with latitude with nearly hemispheric symmetry, were estimated using the model described in Text S4. The independent variable (crater density) is anticorrelated with temperature ($r = -0.64$). As a result, temperature is a confounding variable. To control for temperature, we divided the data set into three latitude ranges (combining N and S latitude bands). The distribution of large craters accounts for a portion of the variability within the selected ranges, which supports our replenishment hypothesis; however, the strength of correlation is such that processes other than impacts must also affect regolith hydrogen content.